Title	Two-petal laser beam near a binary spiral axicon with topological charge 2
Authors	Kotlyar, Victor V.;Stafeev, Sergey S.;Nalimov, Anton G.;Schulz, Sebastian;O'Faolain, Liam
Publication date	2019-06-22
Original Citation	Kotlyar, V. V., Stafeev, S. S., Nalimov, A. G., Schulz, S. and O'Faolain, L. (2019) 'Two-petal laser beam near a binary spiral axicon with topological charge 2', Optics and Laser Technology, 119, 105649 (8pp). doi: 10.1016/j.optlastec.2019.105649
Type of publication	Article (peer-reviewed)
Link to publisher's version	10.1016/j.optlastec.2019.105649
Rights	© 2019, Elsevier Ltd. All rights reserved. This manuscript version is made available under the CC BY-NC-ND 4.0 license. - https://creativecommons.org/licenses/by-nc-nd/4.0/
Download date	2023-05-05 21:20:13
Item downloaded from	http://hdl.handle.net/10468/8150

Two-petal laser beam near a binary spiral axicon with topological charge 2

Victor V. Kotlyar,[1,2] Sergey S. Stafeev,[1,2,*] Anton G. Nalimov[1,2], Sebastian Schulz[3] , Liam O'Faolain[3,4]

[1]*Image Processing Systems Institute—Branch of the Federal Scientific Research Centre "Crystallography and Photonics" of the Russian Academy of Sciences, 151 Molodogvardeyskaya St., Samara 443001, Russia*
[2]*Samara National Research University, 34 Moskovskoye Shosse, Samara 443086, Russia*
[3]*Centre for Advanced Photonics and Process Analysis, Cork Institute of Technology, Cork, Ireland*
[4]*Tyndall National Institute, Cork, Ireland*
**Corresponding author: sergey.stafeev@gmail.com*

We were the first to notice that although in the immediate vicinity of a spiral axicon with m>0 there is no light ring, there is an intensity pattern composed of several intensity petals, whose number is equal to the axicon topological charge, *m*. We experimentally demonstrate that a spiral axicon with the topological charge $m = 2$ and numerical aperture $NA \approx 0.6$, operating at a 532-nm wavelength and fabricated by electron lithography, generates a two-petal (TP) laser beam rotating in the near-field (several micrometers away from the microaxicon surface). The rotation rate attained is higher than any that has been reported to date. It is worth noting that the higher the rotation rate of the TP-beam, the higher the axial resolution of an optical system that can be achieved without increasing its NA. Because a small on-axis shift of a point object leads to a large angle of rotation of its TP-image.

Keywords: Optical vortices, Binary axicon, Laser beam shaping, Rotation of laser beam, FDTD-method, SNOM

1. INTRODUCTION

Rotating light fields, whose transverse intensity distribution is known to rotate about the optical axis upon free-space propagation, have found uses in microscopy for measuring the single-molecule localization and orientation [1], atmospheric sounding and wireless communication systems [2], underwater data transmission [3], and magnetic field sensors [4].

For the first time, rotating optical vortices, presented by coherent light fields with singular phase that experience rotation upon free-space propagation were reported in Refs. [5-7]. A relation for the Laguerre-Gauss (LG) modes whose linear combination generates a rotating intensity pattern while propagating in free space was derived in Ref. [5]. In Ref. [6], a digital hologram was utilized to generate a rotating vortex beam composed of superposition of two LG modes (0,0) and (4,2), and characterized by a two-lobe intensity distribution. The angular rate of rotation of a two-lobe beam (TLB) experimentally measured in Ref. [6] was found to be nonuniform, amounting to 0.008 deg/μm on a linear segment. Rotating laser beams composed of two Bessel modes with the topological charges m= -1 and m= -3 have been generated using a phase diffractive element [7]. The rotation rate was found to be 0.006 deg/μm, with a uniform rotation rate measured in Ref. [7]. The depth of focus (DOF) of an image was precisely measured with a 1.6% error by means of a TLB in Ref. [8]. Using a spatial light modulator, a two-lobe point spread function rotating about the optical axis upon free-space propagation was generated in Ref. [9]. An optimized phase diffractive element was numerically shown to generate a TLB with a 57% efficiency, having demonstrated just a 37% efficiency in the experiment. Being formed with a spherical lens with NA = 0.71, the resulting TLB was composed of a linear combination of multiple LG modes. On a near-focus segment from -1.5 μm to +1.5 μm, the rotation rate of the TLB was 50 deg/μm. In Ref. [10], a TLB composed of two Bessel beams was generated using a

spatial light modulator (SLM), rotating at a rate of 0.003 deg/μm. Accelerated rotation with orbital angular momentum modes has been demonstrated [11]. In particular, using the SLM, a TLB composed of two Bessel modes with $m = 1$ and $m = 3$, rotating at an average rate of 0.0005 deg/μm was generated. Inhomogeneously polarized TLBs were theoretically studied in Ref. [12]. Using a multimode optical fiber, TLBs with different polarization states were generated in Ref. [13, 14, 15]. While being generally nonlinear, the rotation rate was measured to be 0.15 deg/μm on a linear segment of about 10 mm in length. Aberration-unfluenced generation of rotating two-lobe light fields was analyzed in Ref. [14]. The rotation of a four-petal intensity pattern in the cross-section of superposition of two LG beams of opposite handedness with the topological charges m and $-m$ has been analyzed [16]. The rotation rate on a linear section was about 0.0009 deg/μm, with the diffraction pattern found to be surrounded by "spiral wings". A refractive microaxicon 25-μm in diameter has been fabricated in an epoxy film by direct laser-writing with an UV laser diode [17]. It would be challenging to fabricate a spiral axicon using this technique. In Ref. [18], an LG mode with asymmetric defect was generated using an SLM. The resulting incomplete intensity ring was shown to slowly rotate during propagation (having rotated by 0.7 rad at a 20-cm distance). In Ref. [19], using an amplitude computer-generated hologram (CGH), a spiral axicon (m=2) with a spatial carrying frequency was created. The axicon was shown to generate a Bessel beam in the first diffraction order. Using superposition of a Gaussian and a Bessel beam, a slowly rotating TLB was generated (having rotated by 90 deg at a 9.875-cm distance). Two intensity petals in the beam cross-section were shown to be surrounded by "spiral wings". In Ref. [20], using an SLM, a nine-petal coaxial superposition of LG modes with the topological charges 2, 11, and 20 was generated. The intensity pattern was shown to experience a slow rotation upon propagation (having rotated by 10 deg at a 60-cm distance). In Ref. [21], the phase shift of a zero-order Bessel beam was shown to depend in a linear manner on the distance travelled. This explains why the angle of rotation of the superposition of Bessel beams grows linearly with distance. It should be noted that all data relating to the laser beam rotation rates above [1-20] have not been explicitly indicated in the papers but were derived by the present authors from the analysis of the reported results.

Practically significant applications of the TLBs were discussed in Refs. [1-4]. For instance, a scheme of a fluorescent microscope (DOF = 2 μm) offering, respectively, a 250-nm and 500-nm transverse and longitudinal resolution, and the point spread function in the form of two rotating lobes (at a rate of 45 deg/μm) has been proposed [1]. The scheme has enabled the micro-location and orientation of an individual molecule to be identified with a 34-nm accuracy. A relatively stable free-space propagation of a 809-nm TLB over a 1.6-km distance in urban environment (Erlangen, Germany) has been demonstrated [2], with Fried's coherence length being 20 mm. In Ref. [2], the turbulence tolerance of the vortex laser beam was improved by use of a combination of vortex beams, leading to the generation of a multi-petal intensity pattern, instead of the usual intensity ring. In this case, the rotation rate is of no significance. The propagation of a 450-nm multi-lobe optical vortex through underwater turbid environment (attenuation factor $cz = 13$) has been studied [3]. The correlation coefficients after propagating through turbid media was equal to 0.98. In Ref. [4], a rotating TLB experiencing a change in the rotation angle while travelling through a magneto-optical crystal $Bi_4Ge_3O_{12}$ put in a magnetic field was utilized for magnetic field sensing. The sensing technique provided a 28 deg/T sensitivity (T stands for tesla).

We were the first to notice that although in the immediate vicinity of a spiral axicon with m>0 there is no light ring, there is an intensity pattern composed of several intensity petals, whose number is equal to the axicon topological charge, m. The explanation is as follows. A light ring at distance z from the binary SA is formed as the light passes through a spiral turn found at distance $r = z / \tan\theta$ from the optical axis, where θ is the angle of ray tilt behind the axicon. However, at a distance of several wavelengths, the diffraction pattern is formed only by the

central portion of the spiral, from which several turns are originated. It is these initial segments of *m* spiral turns at the center which produce *m* intensity petals. It is after passing through spirals of the binary axicon that the beam acquires the orbital angular momentum. Thus, at distances of several wavelengths from the axicon, the orbital angular momentum causes the intensity pattern of the circularly asymmetric beam to rotate about the optical axis upon propagation.

Practically all above-cited works were concerned with generating a rotating TLB by means of SLM. Meanwhile, if one does not seek to change its parameters, a more efficient way to generate a TLB would be through the use of a diffractive optical element. In this work, using a simple spiral microaxicon with the topological charge $m = 2$ and NA = 0.56, a 532-nm TLB is generated, whose intensity is rotating in the near field on a path segment from 1 μm to 4 μm at a rate of 55 deg/μm. The rotation rate attained is higher than any that has been reported to date. It is worth noting that the higher the rotation rate of the TLB, the higher the axial resolution of an optical system that can be achieved without increasing its NA. Because a small on-axis shift of a point object leads to a large angle of rotation of its two-petal image.

2. THEORETICAL BACKGROUND

For readers' convenience, let us briefly remind of a well-known theory behind the generation of rotating vortex beams [22]. The theory relies on an interference notion because the rotation of the transverse interference pattern is associated with superposition of at least a couple of optical vortices with different topological charges. However, in this work, we propose a spiral axicon that generates a two-lobe transverse intensity pattern not through the interference mechanism but through the diffraction of a plane wave by two spiral branches of a binary surface relief. Because of this, while this theory does not explain the rotation of the two lobes in a straightforward fashion, strange as it may seem, it correctly describes the TLB rotation rate (see Eq. (10)).

It has been demonstrated [22] that rotating laser beams can be generated using an arbitrary known basis of vortex modes (e.g. Laguerre-Gauss, Bessel-Gauss, or Bessel modes, hyper-geometric modes, and so on). The laser beam will be rotating if it is composed from a linear combination of specially fitted modes. Interestingly, different modes will rotate at a different rate. For a beam composed of a linear combination of LG modes, the angle of rotation of the intensity pattern depends on the distance travelled by the beam as follows [22]:

$$\varphi = -B \tan^{-1}\left(z / z_0\right), \tag{1}$$

where

$$B = \frac{2(n-n') + |m| - |m'|}{m-m'} = const, \tag{2}$$

φ is the polar angle in the transverse plane of the beam, the *z*-axis is directed along the optical axis, $z_0 = kw^2/2$ is the Rayleigh range, *k* is the wavenumber of light, *w* is the waist radius of the Gaussian beam, and (*n, m*) are the LG mode numbers, which define the order of the Laguerre polynomial $L_n^{|m|}(x)$. The linear combination can be composed of the LG modes whose numbers (*n, m*) satisfy the condition (2). From (1), the beam is seen to have rotated by an angle of $B\pi/4$ at the distance $z = z_0$, rotating by $B\pi/2$ at large distances *z*. Besides, Eq. (1) suggests that the rotation rate does not remain constant, decreasing with distance *z*.

In a similar way, it is possible to generate a paraxial rotating light beam composed of Bessel modes. Such a beam will have a complex amplitude given by [22]

$$E(r,\varphi,z)=\sum_{n,m}C_{nm}J_m(k\alpha_n r)\exp\left(-ik\alpha_n^2 z/2+im\varphi\right) \quad \textbf{(3)}$$

where C_{nm} are arbitrary complex coefficients, $J_m(x)$ are the m-th order Bessel functions, and α_n is a scale factor of the Bessel function. For the beam with complex amplitude (3) the rotation angle is linearly dependent on z and equal to [22]

$$\varphi = kB_1 z/2 \quad \textbf{(4)}$$

where

$$B_1=\frac{\alpha_n^2-\alpha_{n'}^2}{m-m'}=const. \quad \textbf{(5)}$$

From comparison of (2) and (5) it can be seen that the rotation rate of a beam composed of a linear combination of LG modes can be varied in a discrete manner, by varying the numbers (n, m). Meanwhile, if the rotating beam is composed of a combination of Bessel modes (3), rotation rate (5) can be varied continuously, via varying the scale factor α_n. Another benefit of Bessel modes is that the rotation rate (5) of the resulting beam is constant, meaning that the angle changes linearly with the distance z travelled. Because of this, a measuring device based on Bessel modes is easier to calibrate. Also, note that by increasing the NA of an optical element generating a coaxial superposition of Bessel modes, the distance of linear distance-dependence of the angle can be increased.

An optical scheme for precise estimation of the longitudinal coordinates of an object beyond the diffraction-limited accuracy reported in [1] is based on an imaging system with a rotating double-helix point spread function. The idea is that if a point of an object moves on the optical axis, its image in the form of a double-helix intensity pattern will be rotating about it. Let us recall that the longitudinal resolution of an ideal optical system at half-intensity is given by (DOF = depth of focus) [23]

$$DOF=\frac{\lambda}{2(NA)^2} \quad \textbf{(6)}$$

and the transverse resolution (FWHM= full width at half maximum) is

$$FWHM=\frac{\lambda}{2(NA)} \quad \textbf{(7)}$$

where λ is the incident wavelength. Hence, the technique for measuring the angular motion of two intensity lobes in the transverse plane is more efficient than that based on measuring the intensity pattern motion along the optical axis by a factor of

$$DOF/FWHM=1/NA \quad \textbf{(8)}$$

In practice, the accuracy of the technique is limited by noise in photodetectors [1] and aberrations in optical systems [14]. From (8), it is seen that when measuring the angular rotation of the TLB, the diffraction limit will be overcome to a higher extent for lower-valued NA of the optical system. Hence, for high-NA microscopes (NA = 1) the diffraction limit cannot be overcome using this technique.

In this work, we show that an imaging diffractive optical microelement (a spiral axicon of [24-27] with m = 2) fabricated by electron-beam lithography and reactive ion etching in glass (refractive index $n\approx 1.52$) generates a

TLB that rotates by an angle of 240° on a path segment from 0 μm to 4.5 μm behind the microaxicon. The average rate of the TLB rotation is 55 deg/μm.

3. NUMERICAL SIMULATION

For the first time, an axicon coupled with a spherical lens was proposed as a focuser of light into a narrow ring in [24]. A binary axicon is an annular grating that forms a near-axis zero-order Bessel beam (m=0) [25]. A spiral axicon (SA) with m = 1 has previously been discussed [26]. For the TLB of interest to be generated, a spiral axicon with m = 2 needs to be used.

For a binary SA, the transmission function is:

$$F(r,\varphi) = \mathrm{sgn}\left[\cos\left(k\alpha r + m\varphi\right)\right] \quad \textbf{(9)}$$

where (r,φ) are the polar coordinates and $\mathrm{sgn}(x) = \left(1, x > 0; -1, x < 0\right)$ is the sign function.

Note that an SA with m=2 generates a far-field intensity ring of larger radius when compared with the one from an SA with m=1. Being binary, the SA generates two diffraction orders, with the +1-st order producing a converging wave, resulting in an mth order near-axis Bessel beam, while the -1-st order generates a diverging conical wave with the topological charge $-m$. However several wavelengths away from the SA (in the near-field), there is no intensity ring, with two initial turn segments of two spirals generating two intensity petals, which rotate about the optical axis due to an "asymmetric defect" [18] in the form of asymmetric transmittance of the SA (Fig.1). Figure 1 depicts a binary phase for fabricating the diffractive spiral axicon (9) under study. The spiral axicon in Fig. 1 composed of 15 periods has a period of T_0 = 0.96 μm and the overall radius of R = 15.5 μm. The numerical simulation was conducted for the refractive index n = 1.52 (the axicon and substrate), the incident wavelength λ = 532 nm, and the numerical aperture of the spiral axicon $NA = \lambda/T_0 = 0.56$. The incident wavelength was assumed to be plane and circularly polarized. The simulation parameters were chosen to be the same as they were in the experiment. The microrelief height was H = 0.47 μm and the simulation was conducted for a 15×15×5.1 μm domain with a λ/30 step. This discretization is suffice to enable a simulation error below 1%. The transverse intensity distributions were calculated 4-μm away behind the axicon. The propagation of light through the spiral axicon was numerically simulated using a popular FDTD-aided technique [27-29] implemented in the commercial software. All simulations were carried out using the FullWAVE software (RSoft Software, LightTEC) based on a FDTD method. The size of the grid was λ /30 for all three axes and the time-step was cT=7 nm. The simulation was conducted on a computer with a 1-Tb RAM and two CPU Xeon E5-2699-v4 (22 cores per CPU).

Fig. 1. A phase for fabricating a spiral axicon with m=2: the white spirals are phase π, and the black spirals are the phase of 0.

Figure 2 depicts transverse intensity patterns in certain planes. From Fig. 2, the usual intensity ring is seen to take shape behind the axicon of Fig. 1 only at distances z>8 μm. Meanwhile, for smaller distances, two rotating intensity lobes are observed in the transverse plane. Shown in Fig. 2f is the intensity ring generated in the far-field 58-μm away from the SA.

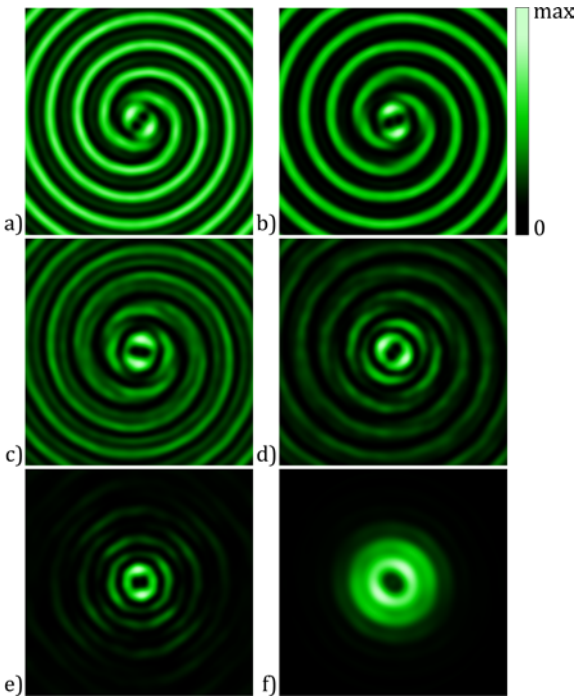

Fig. 2 Numerically simulated (for relief mask depicted in Fig. 1) intensity patterns at a distance of (a) 1 μm, (b) 1.5μm, (c) 2 μm, (d) 4 um, (e) 8μm and (f) 58 um from the axicon surface. The frame size is 8×8 μm. Incident field polarization is left circular.

Figure 3 depicts calculated intensity patterns at the same distances as in Fig. 2, when using the real axicon microrelief shown in Fig. 5a and measured using an atomic-force microscope instead of the ideal relief of Fig. 1. From Fig. 3, we can infer that although fabrication errors (such as trapezoid vs. binary features, underpickling, and others) have led to a distorted diffraction pattern (Fig. 2), two rotating intensity petals are still clearly seen. Alongside two major intensity petals, in Figs. 2 and 3 are also seen other petals, or "spiral wings", associated with other spiral segments. Meanwhile, in the near-field, where the Bessel beam is being formed, there are always additional intensity rings, or spiral wings, contributing to the Bessel beam intensity pattern at larger distances z [30].

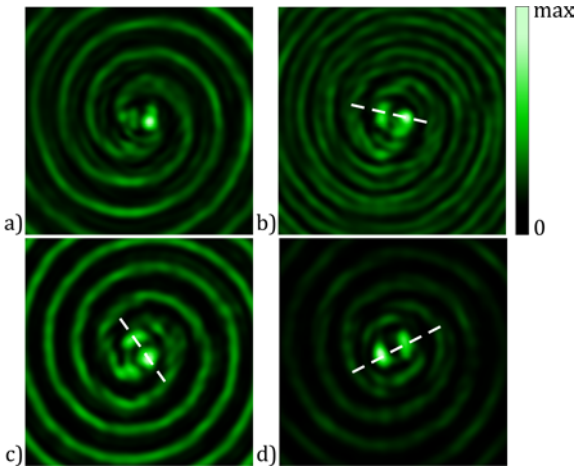

Fig. 3. Numerically simulated intensity patterns at a distance of (a) 1 μm, (b) 1.5μm, (c) 2 μm, and (d) 4μm from the axicon surface (рис. 5a). The frame size is 8×8 μm.

The intensity lobes are spaced ~0.8 μm apart. At the distance of 4 μm (Fig. 3d), they are seen to be oblong and close in size, having a width of FWHMx=0.438μm=0.824λ and a length of FWHMy = 0.57μm=1.07λ. The spiral axicon under analysis operates up to a distance of 9 μm. This can be seen from Fig. 4a, which depicts the intensity profile along the optical axis from a similar axicon, the only difference being the topological number $m = 0$. In Fig. 4, the depth of focus (at full width at half intensity) is DOF = 5.96 μm. Note that the on-axis, behind-the-axicon distance of near-diffraction-free propagation of the beam is independent of the topological charge m (hence, in Fig. 4a we chose m=0). Besides, with the intensity petals rotating during propagation, it is unclear in which way one has to choose an axis parallel to the optical axis z to calculate the intensity. Note that the DOF (where the beam is not diverging) can be increased by increasing the axicon radius R . Figure 4b shows an intensity petal of Fig. 2 to grow near linearly.

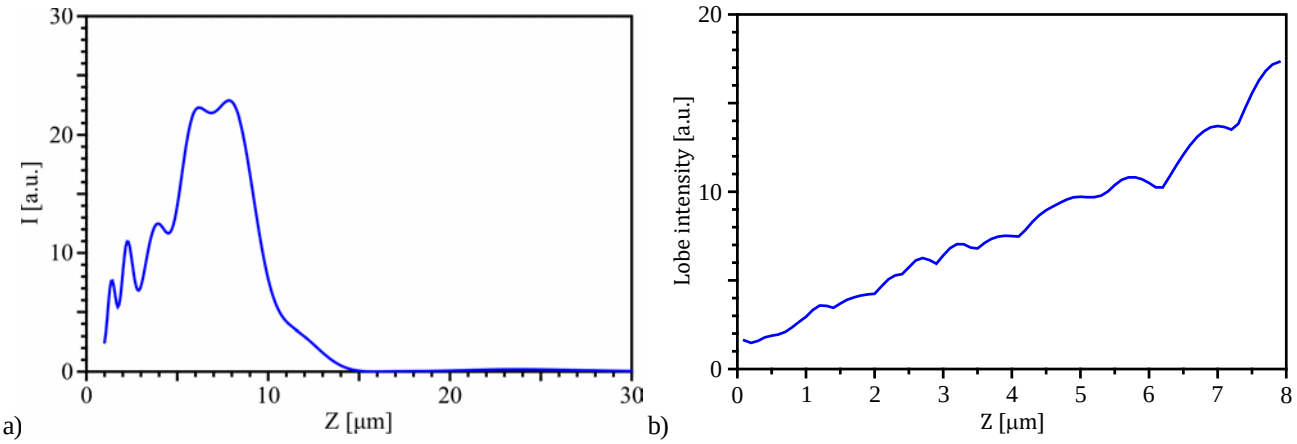

Fig. 4. (a) The on-axis intensity against the distance z for an axicon with m=0 and (b) intensity variation of a petal in Fig. 2. With the intensity ring having been generated at distance z=8 μm, the rotation ceases.

It is worth noting that the intensity ring found 8-μm behind the axicon (Fig. 2e) falls exactly onto the maximum of the on-axis intensity pattern in Fig. 4a. Also, note that the rotation distance of the two-petal pattern cannot be increased by just increasing the aperture radius R, but is possible to increase by increasing the period T_0, though at a trade-off of a decreased rotation rate.

Figure 5 depicts the rotation angle of the intensity lobes in Fig. 2 versus the distance z .

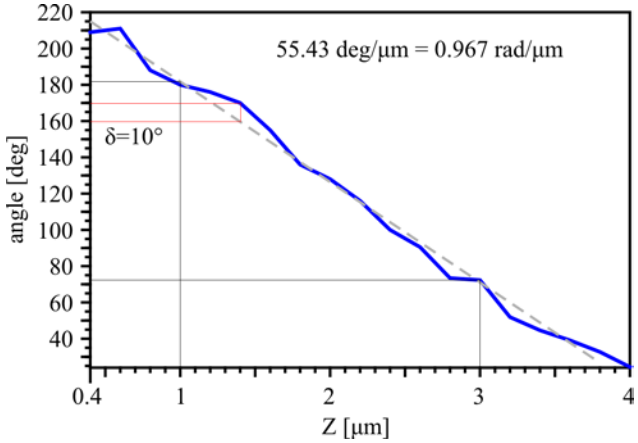

Fig. 5. The rotation angle of the TLB with z ranging from 0.4 μm to 4 μm: the blue solid line shows the results of numerical simulation with a step of z =0.2 μm with the grey dashed line obtained via averaging the tilt of linear sections of the solid line.

From the plot in Fig. 5, the maximum deviation of an individual point from the average line is seen to be not larger than δ=10°. The average angular rate of rotation of TLB maximums is 55.43 deg/μm. The theoretically estimated rate of rotation, derived from (4), is

$$\frac{\varphi}{z} = \frac{k\alpha^2}{2m} \qquad \textbf{(10)}$$

For the axicon, $\alpha = \sin\theta = \frac{\lambda}{T_0}$. This stems from the fact that the scale factor of the Bessel function α in (3) is proportional to half the angle 2θ at the vertex of a spiral conical wave propagating behind the SA and that the binary SA is an annular diffraction grating in which the angle of light diffraction is in inverse proportion to its period. Considering that the modeling and experiment were conducted for λ = 532 nm, m = 2, and T_0 = 0.96 μm, a rotation rate of 53 deg/μm was derived from (10). This is in good agreement with the rotation rate of 55.43 deg/μm derived via the rigorous modeling of the vector diffraction of a laser beam by the spiral axicon. From (10), we can estimate the maximum rotation rate achievable with a diffraction microaxicon. Putting $\alpha = \sin\theta = 1$, Eq. (10) is replaced by $(\varphi / z)_{\max} = k/4 \quad (m = 2)$. Or, $(\varphi / z)_{\max} \approx 180 \text{ deg} / \mu m$. However, one should bear in mind that with increasing rotation rate, the observable rotation distance is decreasing. Simultaneously, the bright spots also decrease in size. With their size becoming equal to the diffraction limit (FWHM=0.5λ) at the maximum numerical aperture (NA=1, T_0= λ), the focal spots get hardly discernible in an optical microscope.

4. FABRICATION AND CHARACTERISATION OF THE SPIRAL AXICON

The SA was fabricated using electron beam lithography in a ZEP520A resist (n=1.52) on a borosilicate glass. This process could be extended to use reactive ion etching and transfer the pattern in the glass. Note that it is possible to synthesize the refractive microaxicon by direct UV-laser writing [17] and the diffractive microaxicon - by photolithography [26]. Meanwhile a high-quality binary microaxicon with a 475-nm width and 400-500-nm depth of the groove can only be synthesized using electron-beam lithography and ion-beam etching.

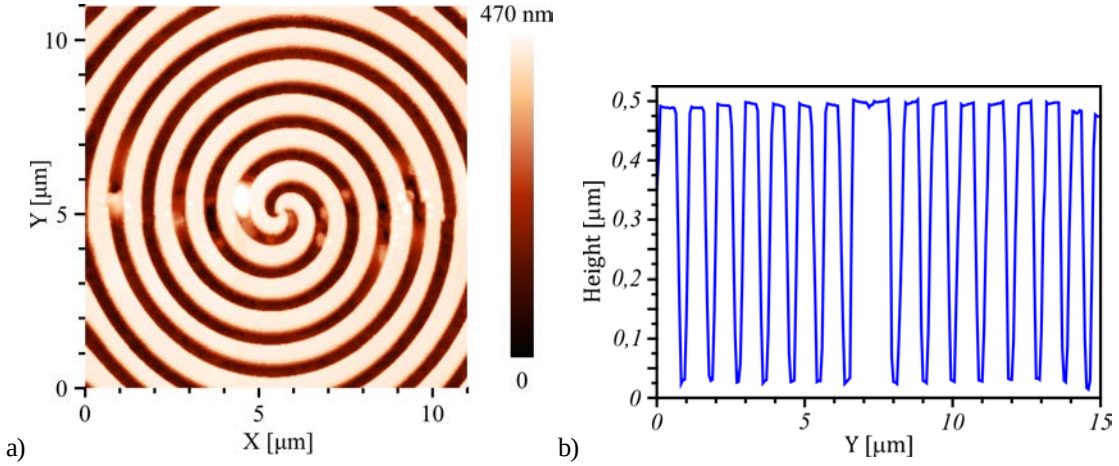

Fig. 6. (a) An image of the SA microrelief with m=2 and (b) its Y-axis profile, both measured with an atomic force microscope.

The central part of the spiral axicon microrelief measured with an atomic force microscope is depicted in Fig. 6. The axicon in Fig. 6b is seen to have a period of T_0 = 0.96 μm and a microrelief feature height of H = 470 nm. This

height is 11% less than the designed height of 532 nm. Note that the height of the binary axicon is chosen so as to attain a half-wavelength phase shift, $H = \lambda / [2(n-1)] \approx \lambda$, where the refractive index is $n = 1.52$. Nonetheless, this fabrication error only leads to a lower efficiency, not affecting the TLB rotation rate, which depends only on the axicon period. The propagation of a circularly polarized beam of wavelength $\lambda = 532$ nm through the fabricated SA with $m = 2$ was then analyzed using a scanning near-field optical microscope (SNOM) Ntegra Spectra (NT-MDT). The intensity of the TLB was measured using a hollow metallized pyramid-shaped tip with a 100-nm pinhole in the vertex. Having passed through the pinhole the light was collected by a 100x objective, before travelling through the spectrometer (Solar TII, Nanofinder 30) to the CCD-camera (Andor, DV401-BV). The SNOM had a 100-nm longitudinal resolution and a 50-nm transverse resolution. A quarter-wave plate had been used to convert a linearly polarized beam into the circularly polarized one. Switching from the left-hand to right-hand polarization was implemented via tilting the quarter-wave plate. Shown in Fig. 7 are transverse intensity patterns measured with a scanning near-field optical microscope at a distance of (a) 1 μm, (b) 1.5 μm, and (c) 2 μm from the SA. The efficiency of the binary microaxicon can be measured only in the far-field, where both diffraction orders jointly produce an intensity ring. The microaxicon can generate the intensity ring with an 80-plus per cent efficiency [31]. However, measuring the efficiency of the binary microaxicon in generating a Bessel beam would present a challenge because the near-axis diffraction pattern at a certain distance z is only contributed to by an axicon fragment shaped as a narrow ring. What is only known [31] is that a binary annular grating generates two conical waves (a diverging and a converging one) with a 40% efficiency. Note that this value is a fortiori higher than the efficiency provided by an SLM (9%-13%) upon recording diffraction gratings with small periods (3 SLM-pixels) [32].

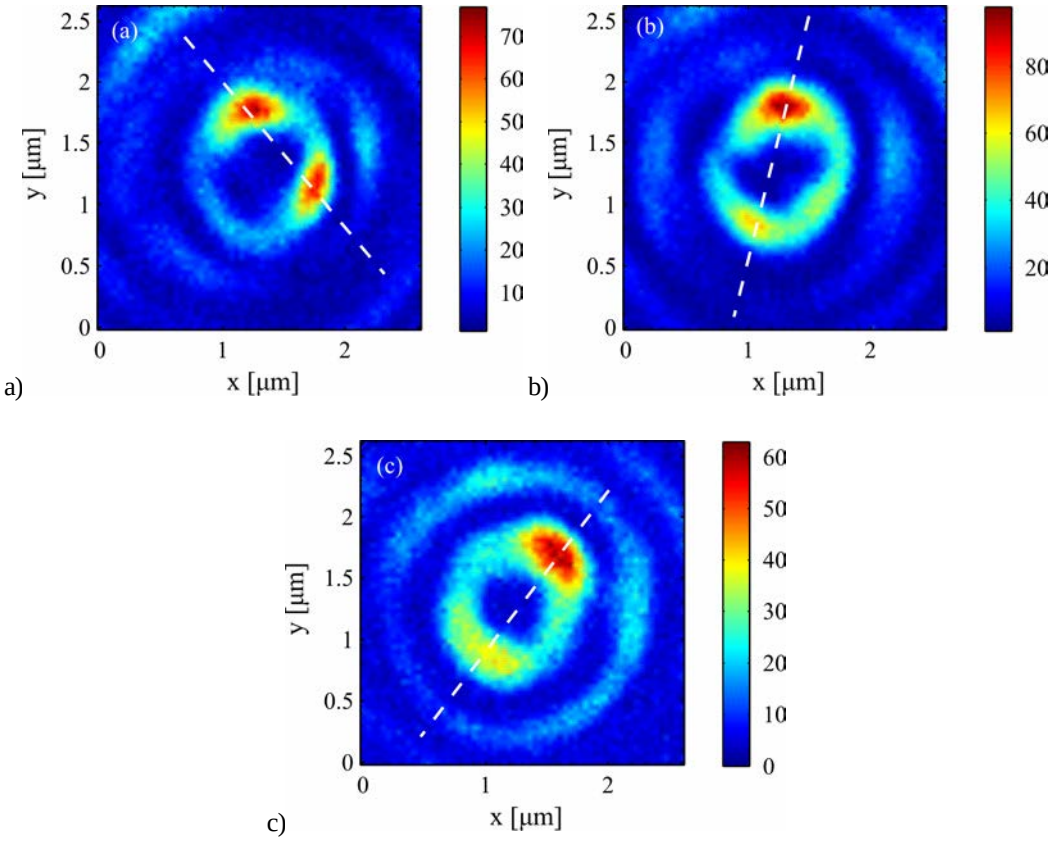

Fig. 7. Transverse intensity patterns measured at a distance of (a) 1 μm, (b) 1.5 μm, and (c) 2 μm for a left-hand circularly polarized incident beam. The dashed line is drawn between the intensity peaks of the two petals.

From Fig. 7, the beam is seen to rotate by nearly 76° after travelling a 1-μm distance. Note that although the difference between the intensity patterns for the right-hand and left-hand circularly polarized TLBs is insignificant, but it still takes place. This is the reason why the SA was illumminated by a circularly, instead or linearly, polarized beam. Shown in Fig. 8a are intensity profiles of the pattern in Fig. 2a, calculated at an angle of 135° (through the maximums of the two lobes), for the left (solid curve) and right (dotted curve) circular polarizations. From Fig. 8a, the intensity lobes are seen to be spaced closer for the right-hand circular polarization than for the left-hand one..

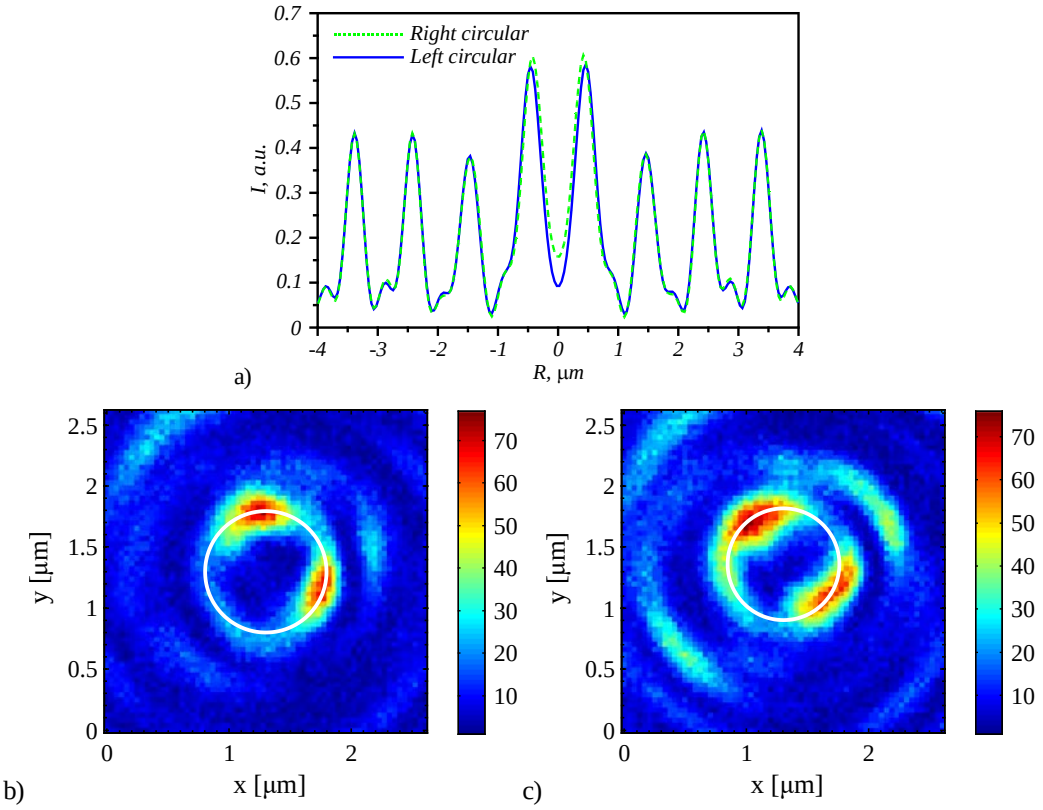

Fig. 8. The profile of the intensity pattern in Fig. 2a, shown at a 135° angle, for the left and right circular polarization, and TLB intensity patterns for the (b) left-hand and (c) right-hand circular polarization of incident light 1-μm behind the SA .

Shown in Figs. 8b and 8c are intensity patterns measured 1-μm behind the axicon (Fig. 6a) for left- and right-hand polarization of incident light. Note that Fig. 8b is identical to Fig. 7a and was reiterated for visual purposes. From the comparison, two main intensity petals in Fig. 8b (left-hand circular polarization) are seen to be located on a larger white circle (0.993-μm diameter) compared to the petals (white circle 0.914-μm diameter) in Fig. 8c (right circular polarization). Hence, we can infer that both the experiment and simulation show that there is a minor difference between the SA-aided intensity patterns generated by the left- and right-hand polarization. The explanation may be as follows. Circular polarization has been known to add/ subtract a unity to/from the topological charge of the optical vortex [33]. In Fig. 1, the topological charge is m=+2. If the microaxicon is illuminated by a right-hand circularly polarized beam, E_x -i E_y, where E_x and E_y are the Cartesian projections of the electric vector, the resulting laser beam will carry the angular momentum proportional to (m-1); whereas under the left-hand circular polarization of incident light, E_x +i E_y, the angular momentum will be proportional to (m+1) [33]. Beams with different topological charge generate different-radius intensity rings: the larger the topological charge, the larger the ring radius (or distance between the main intensity petals). The fact that the radius of the intensity ring increases insignificantly is due to low NA of the axicon (NA=0.56).

Based on intensity measurements at different distances, the *z*-dependence of the TLB rotation angle is plotted in Fig. 9. Note that while the FDTD-aided simulation showed the rotation angle to increase linearly with distance, it was not the case in the experiment. From Fig. 9, the rotation rate is seen to vary not quite linearly, being in good agreement with the numerically simulated rate of 55 deg/μm only on a path section *z* from 1.5 μm to 3 μm. Prior to z = 1.5 μm, the rotation rate is 66 deg/μm, exceeding the numerical estimate (Fig. 5). Meanwhile at distances larger than z = 3 μm, the rotation rate is 34 deg/μm, which is below the numerical estimate.

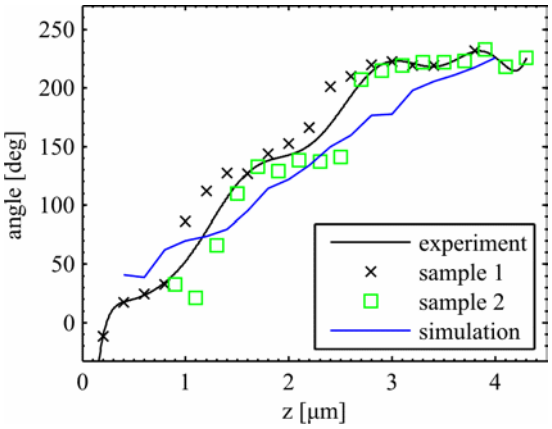

Fig. 9. The rotation angle of the TLB versus the distance to the SA surface. The blue curve shows the result of the FDTD-aided simulation, with the measurements made for two different spiral axicons denoted by markers. The black curve is a fitted curve from the experimental data. The measurement root mean square is ± 2 deg.

The discrepancy between the experimental and calculated curves in Fig. 9 can be explained as follows. In the experiment, for the 30-μm axicon to be entirely illuminated, the microaxicon was placed in the diverging part of the focused Gaussian beam, directly behind its waist. At the same time, the numerical simulation was conducted for a plane incident wave. Because of this, the relation to describe the *z*-dependence of the variation of TLB rotation angle in Fig. 9 is a 'hybrid' between Eq. (4) (linear dependence for a Bessel beam) and Eq. (1) (inverse tangential dependence for a Gaussian beam). This conclusion is in agreement with the results presented in [19], which analyzed the rotation of two intensity petals in coaxial superposition of Bessel and Gauss beams. In other words, rather than using a Bessel beam, a Bessel-Gaussian (BG) beam was generated in the experiment [34]:

$$E(r,\varphi) = J_m(k\alpha r)\exp\left(-r^2 / w^2 + im\varphi\right) \tag{11}$$

It can be shown that for coaxial superposition of BG beams the rotation angle will take the form, instead of Eq. (4):

$$\varphi = kB_1 z\left(1 + z^2 / z_0^2\right)^{-1} / 2 \tag{12}$$

From (12), it follows that in the near-field ($z<<z_0$) the angle varies with distance linearly, as is the case in Eq. (4), but in the far-field ($z>>z_0$), the rotation rate dies away with distance.

CONCLUSION

Considering that the axicon has been known to image an on-axis point as an on-axis line, it is low sensitive to an on-axis shift of a light source. We have proposed a new application of a second-order spiral axicon, via using it as an imaging lens. In this role, the axicon ceases to be insensitive to the on-axis shift of the light source because the

said shifts will lead to the rotation of a two-lobe intensity pattern in the near field behind the axicon. In this study, we reliably detected the rotation of the intensity pattern by an angle of 2º, which corresponds to an no-axis source shift of 500 nm. This magnitude is nearly 2 times smaller than the on-axis resolution of a spherical lens with NA=0.6. Shown in Fig. 10 is a scheme of using spiral axicon as a lens with increased longitudinal resolution. Two insets in it depict TLB rotation by 2 degrees when axial shift is 500 nm.

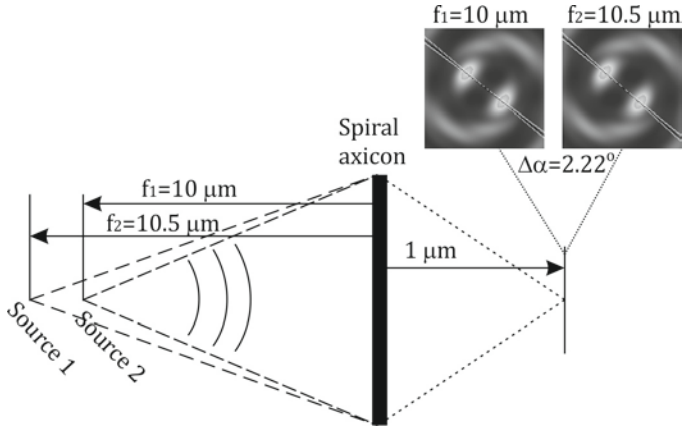

Fig. 10. Optical scheme of using 2-nd order spiral axicon as imaging lens with increased longitudinal resolution

The optical effect theory has elements of novelty because the two light maximums in the intensity pattern have been shown to be formed due to diffraction of light by tails of a double spiral of the axicon binary relief. Meanwhile, their rotation abound the optical axis is explained by the orbital angular momentum that the beam carries due to the spiral form of the axicon binary relief. Offering an analytical description of the near-field diffraction pattern seems to be problematic, at least because the effect is non-paraxial.

It should be noted that optimized diffractive structures intended for obtaining a higher-quality pair of (equal) intensity lobes have been proposed. For instance, in Ref. [9], the authors designed (but did not manufacture) a diffractive optical element (DOE) with NA=0.71, an efficiency of 37%, and a rotation rate of 50 deg/μm over a 3-μm distance. Although the said result is similar to ours, the advantage of our approach is that we have manufactured the element of interest, which is simpler in design and does not need to be calculated using special iterative elements. Into the bargain, while our element is binary, the element of Ref. [9] is multilevel, and while the latter operates in combination with a spherical lens (with the two intensity lobes being generated and rotated near the lens focus), the one proposed in this work operates independently (with the lobes being generated and rotated near the axicon).

We have shown theoretically, numerically, and experimentally that using a simple and well-known microoptics component (a spiral axicon) with low numerical aperture (NA ≈ 0.6) it is possible to generate two-lobe laser beams (at a 55 deg/μm rate) rotating over a certain distance (from 0.5 μm to 4.5 μm) in the axicon vicinity. By measuring the rate of the angular rotation of intensity petals in the transverse plane it is possible to determine the on-axis motion of the object under study, going beyond the diffraction-limited resolution. We have shown (Eq. (8)) that the lower the NA of an optical element that generates the rotating two-lobe beam, the higher the method's efficiency. The spiral axicon may find practical uses for precisely measuring the single-molecule localization and orientation, in atmospheric sounding and wireless communications, as well as in magnetic field sensors.

ACKNOWLEDGEMENTS

Parts of this work were funded as follows. The section "Theoretical background" -- by the Federal Agency for Research Organizations under Agreement 007-ГЗ/Ч3363/26, the "Numerical simulation" -- by the Russian Foundation for Basic Research under grant #16-47-630483, and the "Fabrication of a spiral axicon" -- by the Russian Science Foundation under grant #18-19-00595. Liam O'Faolain and Sebastian Schulz acknowledge funding from the European Research Council (under Starting Grant 337508).

REFERENCES

1. M. P. Backlund, M. D. Lew, A. S. Backer, S. J. Sahl, G. Grover, A. Agrawal, R. Piestun, and W. E. Moerner, "The double-helix point spread function enables precise and accurate measurement of 3D single-molecule localization and orientation," Proc. of SPIE **8590**, 85900L (2013).
2. M. P. J. Lavery, C. Peuntinger, K. Günthner, P. Banzer, D. Elser, R. W. Boyd, M. J. Padgett, C. Marquardt, and G. Leuchs, "Free-space propagation of high-dimensional structured optical fields in an urban environment," Sci. Adv., **3**, 1–8 (2017).
3. K. S. Morgan, J. K. Miller, B. M. Cochenour, W. Li, Y. Li, R. J. Watkins, and E. G. Johnson, "Free space propagation of concentric vortices through underwater turbid environments," J. Opt. **18**, 104004 (2016).
4. S. Yu, F. Pang, H. Liu, X. Li, J. Yang, and T. Wang, "Compositing orbital angular momentum beams in $Bi_4Ge_3O_{12}$ crystal for magnetic field sensing," Appl. Phys. Lett. **111**, 91107 (2017).
5. E. Abramochkin and V. Volostnikov, "Spiral-type beams," Opt. Commun. **102**, 336–350, (1993).
6. Y. Y. Schechner, R. Piestun, and J. Shamir, "Wave propagation with rotating intensity distributions," Phys. Rev. E **54**, R50–R53 (1996).
7. P. Pääkkönen, J. Lautanen, M. Honkanen, M. Kuittinen, J. Turunen, S. N. Khonina, V. V Kotlyar, V. A. Soifer, and A. T. Friberg, "Rotating optical fields," J. Mod. Opt. **45**, 2355–2369 (1998).
8. A. Greengard, Y. Y. Schechner, and R. Piestun, "Depth from diffracted rotation," Opt. Lett. **31**, 181 (2006).
9. S. R. P. Pavani and R. Piestun, "High-efficiency rotating point spread functions," Opt. Express **16**, 3484 (2008).
10. R. R. and I. A. L. and A. Forbes, "Generation and propagation dynamics of obstructed and unobstructed rotating orbital angular momentum-carrying Helicon beams," J. Opt. **14**, 35702 (2012).
11. C. Schulze, F. S. Roux, A. Dudley, R. Rop, M. Duparré, and A. Forbes, "Accelerated rotation with orbital angular momentum modes," Phys. Rev. A **91**, 1–8 (2015).
12. H. Wang, G. Rui, and Q. Zhan, "Dynamic propagation of optical vortices embedded in full Poincaré beams with rotationally polarization symmetry," Opt. Commun. **351**, 15–25 (2015).
13. S. N. Khan, S. K. Chatterjee, and P. R. Chaudhuri, "Polarization and propagation characteristics of switchable first-order azimuthally asymmetric beam generated in dual-mode fiber," Appl. Opt. **54**, 1528, (2015).
14. S. P. Kotova, N. N. Losevsky, D. V. Prokopova, S. A. Samagin, V. G. Volostnikov, and E. N. Vorontsov, "Aberration influenced generation of rotating two-lobe light fields," J. Phys. Conf. Ser. **740**, 012013 (2016).
15. V. G. Volostnikov, E. N. Vorontsov, S. P. Kotova, N. N. Losevsky, D. V Prokopova, E. V Razueva, and S. A. Samagin, "Generation of two-lobe light fields with a rotating intensity distribution under propagation for single emitter spectroscopy," EPJ Web Conf. **132**, 02012 (2017).
16. J. Webster, C. Rosales-Guzman, A. Forbes, "Radially dependent angular acceleration of twisted light," Opt. Lett. **42**, 675-678 (2017).
17. H. Huang, S. Chen, H. Zou, Q. Li, J. Fu, F. Lin, X. Wu, "Fabrication of micro-axicons using direct-laser writing," Opt. Express, **22**, 11035-11042 (2014).
18. J. Humazaki, Y. Mineta, K. Oka, R. Morita, "Direct observation of Gouy phase shift in a propagating optical vortex," Opt. Express, **14**, 8382-8392 (2006).
19. P. Martelli, M. Tacca, A. Gatto, G. Moneta, M. Martinelli ,"Gouy phase shift in nondiffrac vting Bessel beams," Opt. Express, **18**, 7108-7120 (2010).
20. S. Huang, Z. Miao, C. He, F. Pang, Y. Li, T. Wang, "Composite vortex beams by coaxial superposition of Laguerre-Gaussian beams", Opt. Las. Engin.,**78**, 132-139 (2016).
21. M. Kim, T. Scharf, A. C. Assaafrao, C. Rockstuhl, S.F. Periera, H.P. Urbach, H.P. Herzig, "Phase anomalies in Bessel-Gauss beams," Opt, Express, **20**, 28929-28940 (2012).
22. V. V. Kotlyar, S. N. Khonina, R. V. Skidanov, and V. A. Soifer, "Rotation of laser beams with zero of the orbital angular momentum," Opt. Commun. **274**, 8–14 (2007).

23. M. Born and E. Wolf, *Principles of optics* (Pergamon Press, 1968).
24. A. Fedotowsky , K. Lehovec, "Optimal Filter Design for Annular Imaging," Appl. Opt. **13**, 2919-2923 (1974).
25. Y. Kizuka, M. Yamauchi, Y. Matsuoka, "Characteristics of a laser beam spot focused by a binary diffractive axicon", Opt. Engin. **475**, 053401 (2008).
26. S. N. Khonina, V. V. Kotlyar, V. A. Soifer, M. V. Shinkaryev, and G. V. Uspleniev, "Trochoson," Opt. Commun. **91**, 158–162 (1992).
27. A. Taflove, S.C. Hagness, "Computational Electrodynamics: The Finite-Difference Time-Domain Method", Artech House, Boston MA, 2005.
28. N.V. Kantartzis, T.D. Tsiboukis, "Modern EMC Analysis Techniques – Volume 1: Time-Domain Computational Schemes", Morgan & Claypool Publishers, San Rafael CA, 2008.
29. U.S. Ivan, R.A. Marshall, "Numerical Electromagnetics –The FDTD Method", Cambridge University Press, UK, 2011.
30. J. Arlt, K. Dholakia, "Generation of high-order Bessel beams by use of an axicon," Opt. Commun. **177**, 297-301 (2000).
31. O. Livneh, G. Afek, N. Davidson, " Producing an efficient, collimated, and thin annular beam with a binary axicon," Appl. Opt. **57**, 3205-3208 (2018).
32. C. Lingel, T. Haist, W. Osten, "Optimizing the diffraction efficiency of SLM-based holography with respect to the fringing field effect," Appl. Opt. **52**, 6877-6883 (2013).
33. L. Allen, M.W. Beijersbergen, R.J.C. Spreeuw, J.P. Woerdman, " Orbital angular momentum of light and the transformation of Laguerre-Gaussian laser beams," Phys. Rev. A, 45, 8185-8189 (1992).
34. F. Gori, G. Guattari, and C. Padovani, "Bessel-Gauss beams," Opt. Commun. **64**, 491–495 (1987).